The 15 January 2022 Hunga Tonga eruption history as inferred from ionospheric observations

Elvira Astafyeva[1], Boris Maletckii[2], Thomas Dylan Mikesell[3], Edhah Munaibari[4], Michela RAVANELLI[5], Pierdavide Coïsson[2], Fabio Manta[6], and Lucie Rolland[6]

[1]Université Paris Cité, Institut de Physique du Globe de Paris, CNRS UMR 7154
[2]Institut de Physique du Globe de Paris
[3]Norwegian Geotechnical Institute,Boise State University
[4]Université Côte d'Azur, Observatoire de la Côte d'Azur, CNRS, IRD, Géoazur, 250 rue Albert Einstein, Sophia Antipolis 06560 Valbonne, France
[5]Université Paris Cité, Institut de Physique du Globe de Paris, UMR CNRS 7154
[6]Université Côte d'Azur, Observatoire de la Côte d'Azur, CNRS, IRD, Géoazur, 250 rue Albert Einstein, Sophia Antipolis 06560 Valbonne, France.

November 24, 2022

Abstract

On 15 January 2022, the Hunga Tonga-Hunga Ha'apai submarine volcano erupted violently and triggered a giant atmospheric shock wave and tsunami. The exact mechanism of this extraordinary eruptive event, its size and magnitude are not well understood yet. In this work, we analyze data from the nearest ground-based receivers of Global Navigation Satellite System (GNSS) to explore the ionospheric total electron content (TEC) response to this event. We show that the ionospheric response consists of a giant TEC increase followed by a strong long-lasting depletion. We observe that the explosive event of 15 January 2022 began at 04:05:54UT and consisted of at least 5 explosions. Based on the ionospheric TEC data, we estimate the energy released during the main major explosion to be between 9 and 37 Megatons in TNT equivalent. This is the first detailed analysis of the eruption sequence scenario and the timeline from ionospheric TEC observations.

The 15 January 2022 Hunga Tonga eruption history as inferred from ionospheric observations

E. Astafyeva[1], B. Maletckii[1], T. D. Mikesell[2], E. Munaibari[3], M. Ravanelli[1], P. Coisson[1], F. Manta[3], L. Rolland[3]

1 – Université Paris Cité, Institut de physique du globe de Paris (IPGP), 35-39 Rue Hélène Brion, 75013 Paris, France, astafyeva@ipgp.fr
2 – Norwegian Geotechnical Institute, Natural Hazards, Oslo, Norway
3 – Université Côte d'Azur, Observatoire de la Côte d'Azur, CNRS, IRD, Géoazur, 250 rue Albert Einstein, Sophia Antipolis 06560 Valbonne, France.

Keypoints:

- Ionospheric TEC data reveal that the 15 January 2022 Hunga Tonga volcanic eruption involved at least 5 large explosions between 4 and 5UT
- From TEC observations, we estimate the onset time to be 04:05:54UT and the main explosion energy release of 9 to 37 Megatons TNT equivalent
- The eruption-driven shock wave caused an unprecedentedly strong and long-lasting depletion in the ionosphere

Abstract

On 15 January 2022, the Hunga Tonga-Hunga Ha'apai submarine volcano erupted violently and triggered a giant atmospheric shock wave and tsunami. The exact mechanism of this extraordinary eruptive event, its size and magnitude are not well understood yet. In this work, we analyze data from the nearest ground-based receivers of Global Navigation Satellite System (GNSS) to explore the ionospheric total electron content (TEC) response to this event. We show that the ionospheric response consists of a giant TEC increase followed by a strong long-lasting depletion. We observe that the explosive event of 15 January 2022 began at 04:05:54UT and consisted of at least 5 explosions. Based on the ionospheric TEC data, we estimate the energy released during the main major explosion to be between 9 and 37 Megatons in TNT equivalent. This is the first detailed analysis of the eruption sequence scenario and the timeline from ionospheric TEC observations.

Plain Language Summary

On 15 January 2022, the giant explosion of the Hunga Tonga-Hunga Ha'apai volcano shook the atmosphere of the Earth and generated a tsunami. The exact mechanism and timing of the eruption are not well understood yet, nor is the series of events that occurred directly following the first event. Many scientists are trying to understand the chronology of the eruption using different types of data. Here we investigate the signature of the eruption as recorded in Earth's ionosphere, the electrically conductive layer of the atmosphere from about 85-800 km of altitude. We observe variations in the total electron content (TEC) of the ionosphere using Global Navigation Satellite System (GNSS) receivers (commonly known as GPS receivers). Variations in the TEC through time and space are caused by sound waves from the eruption traveling through the ionosphere. We use these variations to constrain the timing of the eruptive events, identifying at least five major explosions during this eruption. In addition, we use the amplitude of TEC variations to estimate that the largest explosion released energy of about 9 to 37 Megaton in trinitrotoluene (TNT) equivalent. This is the first detailed analysis of the eruption scenario and the timeline from ionospheric TEC observations.

Introduction

It is known that volcanic eruptions and explosions generate acoustic and gravity waves that reach the ionosphere and generate so-called co-volcanic ionospheric disturbances (CVIDs; e.g., Astafyeva, 2019; Meng et al., 2019). The ionospheric disturbances are usually registered about 10 to 45 minutes after the eruption onset and are observed directly above the volcano to as far away as 800-1000 km (Heki, 2006; Dautermann et al., 2009; Nakashima et al., 2014; Shults et al., 2016; Manta et al., 2021). CVID often represent quasi-periodic variations of ionospheric electron density or of total electron content (TEC) with periods of 12-30 min (e.g., Dautermann et al, 2009; Shults et al., 2016). The apparent velocity of propagation can vary between 550 m/s and 1100 km/s, which corresponds to gravito-acoustic, acoustic and shock-acoustic waves.

On January 15, 2022, a giant surtseyan volcanic explosion occurred at the uninhabited volcanic island Hunga Tonga-Hunga Ha'apai (HHTH) in South Pacific. The eruption caused the collapse of two-thirds of the volcanic edifice as reported from Sentinel 1 observations (https://marine.copernicus.eu/news/satellites-observe-tsunami-triggered-tonga-volcano), and triggered a tsunami. The interaction between the hot magma and sea water generated a large plume of ash and steam that reached as high as 33-35 km of altitude (e.g., Witze, 2022), and triggered giant atmospheric shock wave that propagated around the world several times (Duncombe, 2022). The eruption also generated large ionospheric disturbances that propagated around the world (Themens et al., 2022; Zhang et al., 2022).

The exact mechanism of the HTHH explosive eruption remains unknown, and the big scientific puzzle is complicated by the fact that the volcano is a submarine and ground-based instruments are not available nearby. Even the eruption onset time is still under debate. Observations from Himawari-8 satellite suggest that the eruption began sometime between 4:00 and 4:10 UT (Gusman and Rodger, 2022). The US Geological Survey (USGS), based on techniques calibrated for earthquakes, estimated that the eruption was equal to a M5.8 earthquake that began at 04:14:45UT (https://earthquake.usgs.gov/earthquakes/eventpage/pt22015050/executive). Poli & Shapiro (2022) based on analysis of long-period surface waves registered by seismic stations, calculated the onset at 04h16m00.07UT. Backprojection of surface pressure data in Tonga estimates the source time at 04:28$\pm$02 UT (Wright et al., 2022).

Here we study the ionospheric response to the HTHH explosion and, for the first time, we reconstruct the timeline of the HTHH eruption sequence fully based on ionospheric observations.

Data and methods

Global Navigation Satellite Systems (GNSS) are nowadays widely used for ionosphere sounding. Phase measurements from dual-frequency GNSS receivers allow to estimate the ionospheric TEC, which is an integrated value equal to the number of electrons along a line-of-sight (LOS) between a satellite and a receiver:

$$sTEC\_ph = \frac{1}{A} \cdot \frac{f_1^2 f_2^2}{f_1^2 - f_2^2} (L_1\lambda_1 - L_2\lambda_2) \tag{1}$$

where A = 40.308 m^3/s^2, L_1 and L_2 are phase measurements, and λ_1 and λ_2 are wavelengths at two GNSS frequencies. For the Global Positioning System (GPS) signals these are: λ_1=1575,42 and λ_2=1227,60 MHz). Most of GNSS (e.g., GPS, Galileo, BeiDou, QZSS) have fixed carrier frequencies. Whereas, in GLONASS each satellite has its own set of frequencies (e.g., Hofmann-Wellenhof et al., 2018; Shults et al., 2016).

In this study, the first data point is subtracted from the whole data series to remove an unknown bias that is always present in the phase measurements., i.e. we are analyzing relative TEC. Further, in order to remove the strong TEC dependence on a LOS elevation angle, we convert the slant TEC to vertical TEC by using the single-layer mapping function (Schaer et al., 1995). The TEC data are displayed in TEC units (TECU), with 1 TECU equal to 10^{16} electrons/m^2.

The spatial positions of ionospheric disturbances are calculated from so-called subionospheric points (SIPs), which are the projections of the intersection points between the LOS and the ionospheric thin shell at a fixed altitude that is often referred to as the altitude of detection *Hion*. Here we take *Hion* = 320 km, which is close to the maximum ionization height HmF2 as derived from the nearest ionosonde station NIUE located at 190.07E; 19.07S (https://lgdc.uml.edu/common/DIDBMonthListForYearAndStation?ursiCode=ND61R&year=2022).

In this study, we analyze non-filtered TEC data, in order to keep the amplitude of the signal and temporal characteristics unchanged. This also enables to better investigate the link between the eruption features and the ionospheric response. We use 30-sec data.

Results & Discussion

During the eruption, 15 ground-based GNSS-receivers were operational within ~2000 km distance from the volcano (Figure 1a). Most of these receivers captured signals from GPS (code "G"), GLONASS (code "R"), Galileo (code "E"), Beidou (code "C"), SBAS (code "S") and QZSS (code "J") satellite constellations. The following satellites showed clear CVID signatures in the ionospheric TEC data: G10, G18, G23, G24, G32, R07, R20, R21, E03, E36, C01, C04, C23, C24, C25, C27, C28, S33 (Figure 1b). In addition, a few stations captured signals from J01, J02, J03, J04 and J07 satellites. Such an impressive number of observation points allowed us to analyze the CVID evolution with an unprecedented level of detail.

1. TEC variations of unprecedented amplitude due to shock waves

The ionospheric TEC data series registered near the volcano are presented in Figure 1(c-f). The first CVID signatures are visible at ~4.45UT, while several other large variations are seen at later times. Interestingly, these TEC variations do not represent the "classic" quasi—periodic waveform observed in previous studies. These CVID are complex waveforms with a clear occurrence of N-waves with very sharp TEC increases, which is an indication of an acoustic or shock-acoustic wave source. Similar disturbances were observed following the giant M9 March 2011 Tohoku-Oki earthquake (e.g., Astafyeva et al., 2011; Liu et al., 2011).

The other remarkable observation is the amplitude of the TEC response to the HTHH eruption that reaches the extraordinary level of 5-8 TECU (Figure 1c-1f). Given the absolute background vertical TEC around the volcano varies from 18 to 23 TECU at the beginning of the eruption, we conclude that the CVID contribution to the background TEC is 21-44 %. This value is unprecedented with respect to previous studies that showed ~8% for eruptions with volcanic explosivity index (VEI) of 2, and 15-18% for VEI=4 eruptions (Shults et al., 2016).

2. Multiple volcanic explosions are detected by the ionosphere

We note that the TEC variations show multiple large peaks occurring between 4.45 and 5.6 UT (Figure 1c-f and Figure 2a). We propose that these individual peaks represent individual explosions that occurred between 4 and ~5UT (Figure 2b). The acoustic or shock-acoustic nature of the observed peaks can be confirmed from the N-type waveforms of the CVID and their apparent velocities (Figure S2). A similar complex TEC response was observed for the largest M9 earthquakes, driven by multiple rupturing segments of the megathrust fault: the 2011 Tohoku-Oki (Astafyeva et al., 2013b) and the 2004 Sumatra earthquake (Heki et al., 2006).

The scenario of multiple explosions is in line with conclusions by Wright et al. (2022) made from the analysis of surface pressure data recorded at a station in Tonga, only 64 km away from the HTHH volcano. Wright et al. (2022) identified the first peak at 04:26UT and four other events at 04:36UT, 05:10UT, 05:51UT and 08:46UT.

From the ionosphere, we can estimate the onset time by approximating CVID propagation as a spherical wave at a constant speed from a point source (Figure S1a; Kiryushkin and Afraimovich, 2007). Shults et al. (2016) used such an approximation to locate the eruptive source position fully based on ionospheric data. Here, we modify the previous algorithm by fixing the source at the volcano position and by only varying the CVID radial speed in order to obtain the most probable onset time (Text S1). From TEC data, we select peaks with clear N-wave-like waveforms that could represent explosions. For each event, we determine the CVID arrival times at the moment when the TEC starts to increase suddenly (Figure S1b), and the coordinates of the CVID detection (Tables S1,S2,S3,S4,S5). From these data and by applying our method, we obtain the following onset times for the five sub-events/explosions (Figure 2a): event #1 that lead to the preparation of the big explosions and the caldera collapse, began at 04:08:43UT. The largest two explosions occurred at 04:20:00 UT and at 04:28:05UT, then smaller sub-events took place at 04:48:30UT (#4) and at 04:55:21 UT (#5) (Table 1). We note that other TEC peaks were analyzed but did not give a solution. We therefore consider that they are not of acoustic nature.

To confirm these proposed event times and multiple events scenario, we model individual explosive events using the IonoSeis package (Rolland et al., 2013, Mikesell et al., 2019). This model uses one-dimensional sound speed and density profiles (Figure 3a, 3b, respectively) based on the local date and time computed with NRLMSIS 2.0 (Emmert et al., 2020). The model uses a threedimensional background electron density profile based on local date and time (IRI2016, Bilitza et al., 2017), as well as the local magnetic field inclination and declination (IGRF, Thébault et al., 2015). IonoSeis propagates an acoustic N-shaped pulse through the atmosphere from the location of the volcano at the Earth's surface to the ionosphere (Dessa et al., 2005). The neutral atmospheric wave is coupled into the ionosphere model and the slant TEC variation between satellite-receiver is computed (Mikesell et al., 2019). More details about the parameters chosen in this study can be found in Text S2 (Supplementary Material).

To reproduce the TEC series observed after the HTHH volcano explosion, five pulses of different amplitude were launched at different moments of time (Figure 3c). The modelling results confirm the occurrence of at least 5 explosions and also that events #2 and #3 were the largest. The simulations also provide us with another set of the onset times: the initial explosion (trigger) at 04:03:15UT, the main big explosion at 04:16:20UT, another big one at 04:24:45UT, and events #4 and #5 at 04:24:45UT and 05:02:15UT, respectively. The IonoSeis onsets are always 3.5-4.5 min ahead of those estimated by the spherical approximation method (Table 1), which can be explained by the difference in the approaches (constant velocity in the first method and a 1D velocity varying with altitude in the IonoSeis). Also, the spherical wave method is based on the manual determination of the arrival time, which can introduce additional inaccuracy. Knowing that IonoSeis tends to systematically delay the arrival of disturbance with respect to observations (Lee et al., 2018; Mikesell et al., 2019; Zedek et al., 2021), we provide the final ionospheric solution for the onset times by averaging the solutions by two ionospheric methods (Table 1). We obtain 04:05:54$\pm$169s UT for the onset HTHH eruption trigger event and 04:18:10$\pm$110 UT for the main big explosion.

3. Explosion energy release as estimated from the ionosphere

From the ionospheric GNSS-derived TEC data it is possible to estimate the energy of the volcanic explosion (Heki, 2006; Dautermann et al, 2009). Heki (2006) suggested an empirical method based on analysis of CVID amplitudes with respect to the background TEC and comparison of the TEC response to Wyoming mine blasts of known explosive power by Calais et al. (1998). In that latter case, the explosion power of 1,5 kiloton in TNT equivalent generated TEC disturbance with the maximum amplitude of 0.03 TECU on the background absolute VTEC of 10.6 TECU. By using this method, Heki (2006) estimated the energy of the VEI=2 Asama volcano explosion as of ~4×10^4 t TNT or 2×10^{14} Joule. However, it is important to note that besides the background TEC, other two factors affect the amplitude of CVID: the magnetic field configuration and the angle between the LOS and the disturbance wavefront (Otsuka et al., 2006; Kakinami et al., 2013; Rolland et al., 2013; Bagiya et al., 2019). Therefore, these parameters should be taken into account when comparing the disturbance amplitudes on the day of the Wyoming blast and the HTHH explosion.

In our case, multiple LOS on the north-west and north-east from the volcano detect CVID with similar amplitudes of 5-8 TECU, therefore, we conclude that the impact of the LOS-wavefront intersection is less important for such a huge event. Therefore, the rough estimation of the energy release is estimated by taking the maximum CVID amplitudes 5 and 8 TECU (at *samo-E03, usp1-G24*, *ftna-G24*, *ftna-E36*, *samo-R20*), and the background TEC (between 18 and 23 TECU). Knowing that the wave energy scales with the square of the amplitude, we estimate that the HTHH explosion is about 5900 and 24700 times more powerful than the mine blasts studied by Calais et al. (1998).

Therefore, the HTHH explosion power is between ~9 and 37 megaton (Mt) in TNT equivalent, or between ~3.7×10^{16} and 1.5×10^{17} J. This value is in agreement with estimations from other instruments and methods between 4 and 18 Mt of TNT (Garvin, 2022), and it is of the order of the 1883 Krakatoa volcano explosion, for which the acoustic energy was estimated as high as $8.6*10^{16}$ J (Woulff and McGretchun, 1976). The fact that the HTHH explosion generated a huge Lamb wave that travelled around the world at least 3 times (e.g., Zhang et al., 2022) is additional indication of the similar energy release with the Krakatoa explosion.

4. The giant and long-lasting ionospheric hole

In Figures 1c-1f, we notice an abrupt decrease in TEC starting from ~4.7 UT. This decrease is clearly observed by comparing the event data series to four quiet days preceding the eruption (10 to 13 January 2022) and the day after (Figure 4). Although we see day-to-day variations, the depletion is only present on 15 January. This ionospheric depletion (“hole”) resembles TEC response to the Tohoku-Oki earthquake and several other large earthquakes (e.g., Kakinami et al., 2012; Astafyeva et al., 2013a). Astafyeva et al. (2013a) demonstrated that the magnitude and the duration of the depletion scales with the magnitude of an earthquake and explained the hole as the rarefaction phase of the shock-acoustic wave. For the 2011 Tohoku-Oki earthquake, the depletion lasted 30-50 min and the TEC decreased by -5 to -6 TECU with respect to the before-earthquake level (Astafyeva et al., 2013a,b). In the case of the HTHH event, the depletion of the amplitude of -13-18 TECU lasted for at least 1.5-2 hours (Figure 4), which is unprecedented, both in magnitude and duration. This could be explained, first of all, by the fact that eruptive explosions should generate stronger shock waves than earthquakes because the source is located at shallow depth (about 200 m) under water but not underground. The giant shock wave would cause large-amplitude and long-lasting rarefaction phase. Similarly, Aa et al. (2022) suggested that the depletion was composed of cascading TEC decreases due to different acoustic wave impulses.

Second, it is possible that the HTHH ionospheric depletion was reinforced by a geomagnetic storm that began several hours before the eruption, and was in an early recovery phase at the time of the CVID observations. While the storm was moderate (minimum Dst excursion of -100 nT, World Data Center for Geomagnetism, 2015), the storm-time composition changes were significant, as the data of the Global Ultraviolet Imager (GUVI) onboard the Thermosphere, Ionosphere, Mesosphere Energetics and Dynamics (TIMED) satellite (http://guvitimed.jhuapl.edu/, Christensen et al., 2003) show (Figure S3). The O/N2 ratio was reduced above the area of the CVID observations, which means decreased ionization (e.g., Prölss, 1976).

Third, unlike the Tohoku-Oki earthquake that occurred in the local afternoon, the HTHH depletion developed during local evening hours, which undoubtedly also have played a role in the retarded recovery from the hole because of the decreased evening ionization level.

The extremely low local ionization level due to the depletion made it difficult to clearly detect and to analyze one later eruption that took place around 8:30UT (Figure S4; Wright et al., 2022).

Conclusions

The extraordinary Hunga Tonga-Hunga Ha’apai volcano eruption and related explosive events generated quite significant and long-lasting effects in the ionosphere. Shortly after the eruption onset, GNSS-receivers around the volcano area showed TEC variations with several distinct peaks that correspond, most likely, to a trigger event (the initial explosion) at 04:05:54±169s UT and 4 other explosions that occurred between 4:18 and 4:54UT on 15 January 2022.

The second and the most powerful explosion occurred at 04:18:10UT. Based on the CVID amplitudes and the background TEC value, we estimate that this major explosion released energy between 9 and 37 Megaton in TNT equivalent, that is comparable to the 1883 Krakatoa event.

The large TEC increase was followed by major depletion in the ionosphere in the vicinity of the volcano. The TEC dropped by -13 to -18 TECU below the quiet TEC values, and the depletion lasted for at least 1,5-2 hours, which is unprecedented. The depletion was primarily caused by the giant shock waves, and represents the rarefaction phase of the giant CVID.

We demonstrate that numerous ionospheric sounding points in the vicinity of the volcano can help to decipher the eruption scenario and chronology. This is the first study of the kind.

Open Research

All GNSS data are available from the CDDIS archives https://cddis.nasa.gov/Data_and_Derived_Products/GNSS/daily_30second_data.html and data of RAUL station are from the Geological hazard information for New Zealand (GeoNet) database via https://data.geonet.org.nz/gnss/rinex/2022/015/. The thermospheric O/N2 composition data are available from: http://guvitimed.jhuapl.edu/guvi-galleryl3on2. The TEC estimation "tec-suite" codes are accessible from https://tec-suite.readthedocs.io/en/latest/installation.html. The GMT6.0 software is available at https://www.generic-mapping-tools.org/download/.

Acknowledgement

This work was supported by the French Space Agency (CNES), projects "RealDetect" (EA, BM) and "UV-TECGEOX" (LR, EM). LR, EM and TDM acknowledge the support of the French National Agency of Research (ANR), project ITEC (grant ANR-19-CE04-0003), and project Université Côte d'Azur Investissement d'Avenir Idex. MR, EM and MB thank the CNES for the PhD and PostDoctoral Fellowships. We thank I. Zhivetiev for the "tec-suite" codes. Figures were done by using the GMT6.0 software (Wessel et al., 2019).

References

Aa, E., S.-R. Zhang, et al. (2022) Significant equatorial plasma bubbles and global ionospheric disturbances after the 2022 Tonga volcano eruption, *ESSOAr*, Doi: 10.1002/essoar.10510637.1, https://www.essoar.org/doi/abs/10.1002/essoar.10510637.1

Astafyeva, E. (2019) Ionospheric detection of natural hazards. *Reviews of Geophysics,* **57(4)**, 1265-1288. https://doi.org/10.1029/2019RG000668.

Astafyeva, E., P. Lognonné, L. Rolland (2011), First ionosphere images for the seismic slip on the example of the Tohoku-Oki earthquake. *Geophys. Res. Lett.*, V.38, L22104, DOI:10.1029/2011GL049623.

Astafyeva, E., S. Shalimov, E. Olshanskaya, P. Lognonné (2013a) Ionospheric response to earthquakes of different magnitudes: larger quakes perturb the ionosphere stronger and longer. *Geophys. Res. Lett*., V.40, N9, 1675-1681, DOI: 10.1002/grl.50398.

Astafyeva, E., L. Rolland, P. Lognonné, K. Khelfi, T. Yahagi. (2013b) Parameters of seismic source as deduced from 1Hz ionospheric GPS data: case-study of the 2011 Tohoku-Oki event. *J. Geophys. Res.,* V. 118, 9, 5942-5950. DOI:10.1002/jgra50556.

Bagiya et al. (2019) Mapping the Impact of Non-Tectonic Forcing mechanisms on GNSS measured Coseismic Ionospheric Perturbations. *Sci. Reports.* 9:18640, doi:10.1038/s41598-019-54354-0.

Bilitza, D., Altadill, D., Truhlik, V., Shubin, V., Galkin, I., Reinisch, B., & Huang, X. (2017). International Reference Ionosphere 2016: From ionospheric climate to real-time weather predictions. Space Weather, 15, 418–429. https://doi.org/10.1002/2016SW001593

Calais, E., J. B. Minster, M. A. Hofton, and H. Hedlin (1998), Ionospheric signature of surface mine blasts from Global Positioning System measurements, *Geophys. J. Int.*, 132, 191– 202.

Christensen, A. B., et al. (2003), Initial observations with the Global Ultraviolet Imager (GUVI) on the NASA TIMED satellite mission, *J. Geophys. Res*., 108(A12), 1451, doi:10.1029/2003JA009918.

Dautermann, T., E. Calais, and G. S. Mattioli (2009), Global Positioning System detection and energy estimation of the ionospheric wave caused by the 13 July 2003 explosion of the Soufrière Hills Volcano, Montserrat, *J. Geophys. Res*., 114, B02202, doi:10.1029/2008JB005722.

Dessa, J. X., Virieux, J., & Lambotte, S. (2005). Infrasound modeling in a spherical heterogeneous atmosphere. *Geophysical Research Letters*, *32*(12), 1–5. https://doi.org/10.1029/2005GL022867

Duncombe, J. (2022), The surprising reach of Tonga's giant atmospheric waves, *Eos, 103,* https://doi.org/10.1029/2022EO220050. Published on 21 January 2022.

Emmert, J. T., Drob, D. P., Picone, J. M., Siskind, D. E., Jones, M. Jr., Mlynczak, M. G., et al. (2020). NRLMSIS 2.0: A whole-atmosphere empirical model of temperature and neutral species densities. *Earth and Space Science*, 7, e2020EA001321. https://doi.org/10.1029/2020EA001321

Fuller-Rowell, T. J., Codrescu, M. V., Moffett, R. J., & Quegan, S. (1994). Response of the thermosphere and ionosphere to geomagnetic storms. *Journal of Geophysical Research*, 99(A3), 3893–3914. https://doi.org/10.1029/93JA02015

Garvin, J. (2022). Dramatic Changes at Hunga Tonga-Hunga Ha'apai. Available at: https://earthobservatory.nasa.gov/images/149367/dramatic-changes-at-hungatonga-hunga-haapai

Gusman, A.R. & Roger, J. (2022). Hunga Tonga - Hunga Ha'apai volcano-induced sea level oscillations and tsunami simulations. GNS Science webpage, https://doi.org/10.21420/DYKJ-RK41

Heki, K. (2006), Explosion energy of the 2004 eruption of the Asama Volcano, central Japan, inferred from ionospheric disturbances, *Geophys. Res. Lett.*, 33, L14303, doi:10.1029/2006GL026249.

Heki, K., Y. Otsuka, N. Choosakul, N. Hemmakorn, T. Komolmis, and T. Maruyama (2006), Detection of ruptures of Andaman fault segments in the 2004 great Sumatra earthquake with coseismic ionospheric disturbances, *J. Geophys. Res.*, 111, B09313, doi:10.1029/2005JB004202.

Hofmann-Wellenhof, B., H. Lichtenegger & E. Wasle. (2008) GNSS-Global Navigation Satellite Systems. *Springer, Vienna*, https://doi.org/10.1007/978-3-211-73017-1

Kakinami, Y. et al. (2012) Tsunamigenic ionospheric hole, *Geophys. Res. Lett.*, 39, L00G27, doi:10.1029/2011GL050159.

Kakinami et al. (2013), Ionospheric ripples excited by superimposed wave fronts associated with Rayleigh waves in the thermosphere*, J. Geophys. Res.*, doi:10.1002/jgra.50099.

Kiryushkin, V.V. and E.L. Afraimovich (2007) Determining the Parameters of Ionospheric Perturbation Caused by Earthquakes Using the Quasi-Optimum Algorithm of Spatiotemporal Processing of TEC Measurements, *Earth Planets Space*, 2007, vol. 59, pp. 267–278.

Lee, R. F., Rolland, L. M., & Mikesell, T. D. (2018). Seismo-Ionospheric Observations, Modeling, and Backprojection of the 2016 Kaikōura Earthquake. *Bulletin of the Seismological Society of America*, *108*(3B), 1794–1806. https://doi.org/10.1785/0120170299

Manta, F., G. Occhipinti, E. Hill, A. Perttu, B. Taisne (2021) Correlation Between GNSS-TEC and Eruption Magnitude Supports the Use of Ionospheric Sensing to Complement Volcanic Hazard Assessment, *J. Geophys. Res. - Solid Earth*, doi:10.1029/2020JB020726

Meng, X., Vergados, P., Komjathy, A., & Verkhoglyadova, O. (2019) Upper atmospheric responses to surface disturbances: An observational perspective. *Radio Science* **54**, 1076 – 1098. https://doi.org/10.1029/2019RS006858

Mikesell, T.D.; Rolland, L.M.; Lee, R.F.; Zedek, F.; Coïsson, P.; Dessa, J.-X. (2019) *IonoSeis*: A Package to Model Coseismic Ionospheric Disturbances. *Atmosphere*, *10*, 443. https://doi.org/10.3390/atmos10080443

Nakashima, Y., K. Heki, A. Takeo, M.N. Cahyadi, A. Aditiya, K. Yoshizawa. (2016) Atmospheric resonant oscillations by the 2014 eruption of the Kelud volcano, Indonesia, observed with the ionospheric total electron contents and seismic signals. *Earth and Planetary Science Letters*, V. 434, 112-116, doi:10.1016/j.epsl.2015.11.029.

Otsuka et al. (2006), GPS detection of total electron content variations over Indonesia and Thailand following the 26 December 2004 earthquake, *Earth Planets Space*, 58, 159-165, doi: 10.1186/BF03353373.

Poli, P. and M. Shapiro (2022) Rapid characterization of large volcanic eruptions: measuring the impulse of the Hunga Tonga explosion from teleseismic waves. *Geophys. Res. Letters,* V. 49, e2022GL098123, doi: 10.1029/2022GL098123

Prölss, G. W. (1976) On explaining the negative phase of ionospheric storms, Planet. Space Sci., 24, 607-609.

Rolland, L. M., M. Vergnolle, J.-M. Nocquet, A. Sladen, J.-X. Dessa, F. Tavakoli, H.R. Nankali, and F. Cappa (2013), Discriminating the tectonic and non-tectonic contributions in the ionospheric signature of the 2011, Mw7.1, dip-slip Van earthquake, Eastern Turkey, *Geophys. Res. Lett.*, 40, doi:10.1002/grl.50544.

Schaer, S., G. Beutler, L. Mervart, M. Rothacher (1995) Global and regional ionosphere models using the GPS double difference phase observable, *Proceedings of the 1995 IGS Workshop, Potsdam, Germany, May 15–17, 1995.* https://mediatum.ub.tum.de/doc/1365730/137709.pdf

Shults, K., E. Astafyeva and S. Adourian (2016). Ionospheric detection and localization of volcano eruptions on the example of the April 2015 Calbuco events. *J. Geophys. Res. -Space Physics*, V.121, N10, 10,303-10,315, doi:10.1002/2016JA023382.

Thébault, E.; Finlay, C.C.; Beggan, C.D.; Alken, P.; Aubert, J.; Barrois, O.; Bertrand, F.; Bondar, T.; Boness, A.; Brocco, L.; et al. Wardinski, I.; Zvereva, T. (2015) International Geomagnetic

Reference Field: The 12th generation. Earth Planets Space, 67, 79, doi:10.1186/s40623-015-0228-9

Themens, D. R., Watson, C., Žagar, N., Vasylkevych, S., Elvidge, S., McCaffrey, A., et al. (2022). Global propagation of ionospheric disturbances associated with the 2022 Tonga Volcanic Eruption. *Geophysical Research Letters*, 49, e2022GL098158. doi.org: 10.1029/2022GL098158

Wessel, P., J.F. Luis, L. Uieda, R. Scharroo, F. Wobbe, W.H.F. Smith, D. Tian (2019) The Generic Mapping Tools Version 6. *Geochemistry, Geophysics, Geosystems*. V. 20, N11, Doi: 10.1029/2019GC00851

Witze, A. (2022) Why the Tongan volcanic eruption was so shocking. *Nature*, Vol.602, p. 376-378. doi: d41586-022-00394 https://media.nature.com/original/magazine-assets/d41586-022-00394-y/d41586-022-00394-y.pdf.

World Data Center for Geomagnetism, Kyoto, M. Nose, T. Iyemori, M. Sugiura, T. Kamei (2015), Geomagnetic Dst index, http://wdc.kugi.kyoto-u.ac.jp/dst_realtime/202201/index.html, doi: 10.17593/14515-74000.

Wright, C.J., et al. (2022) Tonga eruption triggered waves propagating globally from surface to edge of space, *ESSOAr*, https://www.essoar.org/pdfjs/10.1002/essoar.10510674.1

Woulff, G., and T. R. McGetchin (1976), Acoustic noise from volcanoes—Theory and experiment, *Geophys. J. R. Astron. Soc.*, 45, 601–616.

Zedek, F., Rolland, L. M., Mikesell, T. D., Sladen, A., Delouis, B., Twardzik, C., & Coïsson, P. (2021). Locating surface deformation induced by earthquakes using GPS, GLONASS and Galileo ionospheric sounding from a single station. *Advances in Space Research*, *68*(8), 3403–3416. https://doi.org/10.1016/j.asr.2021.06.011

Zhang S-R, Vierinen J, Aa E, Goncharenko LP, Erickson PJ, Rideout W, Coster AJ and Spicher A (2022) 2022 Tonga Volcanic Eruption Induced Global Propagation of Ionospheric Disturbances via Lamb Waves. *Front. Astron. Space Sci*. 9:871275. doi: 10.3389/fspas.2022.871275.

Figure Captions

Figure 1. (a) The geometry of CVID observations by multiple GNSS. Black squares show the GNSS stations, the red star depicts the volcano (175.382W; 20.53S), blue triangle - the ionosonde station; **(b)** IPP trajectories for the station FTNA at the altitude *Hion*=320 km, for the time period between 4:14 (the USGS eruption time onset) and 8UT. Satellite names are shown at the beginning of each IPP trajectory that corresponds to the eruption onset; **(c-f)** Ionospheric TEC variations registered by the four closest GNSS receivers: *tong* **(c)**, *usp1* **(d)**, *ftna* **(e)** and *samo* **(f)**. Names of satellites are noted on the panels.

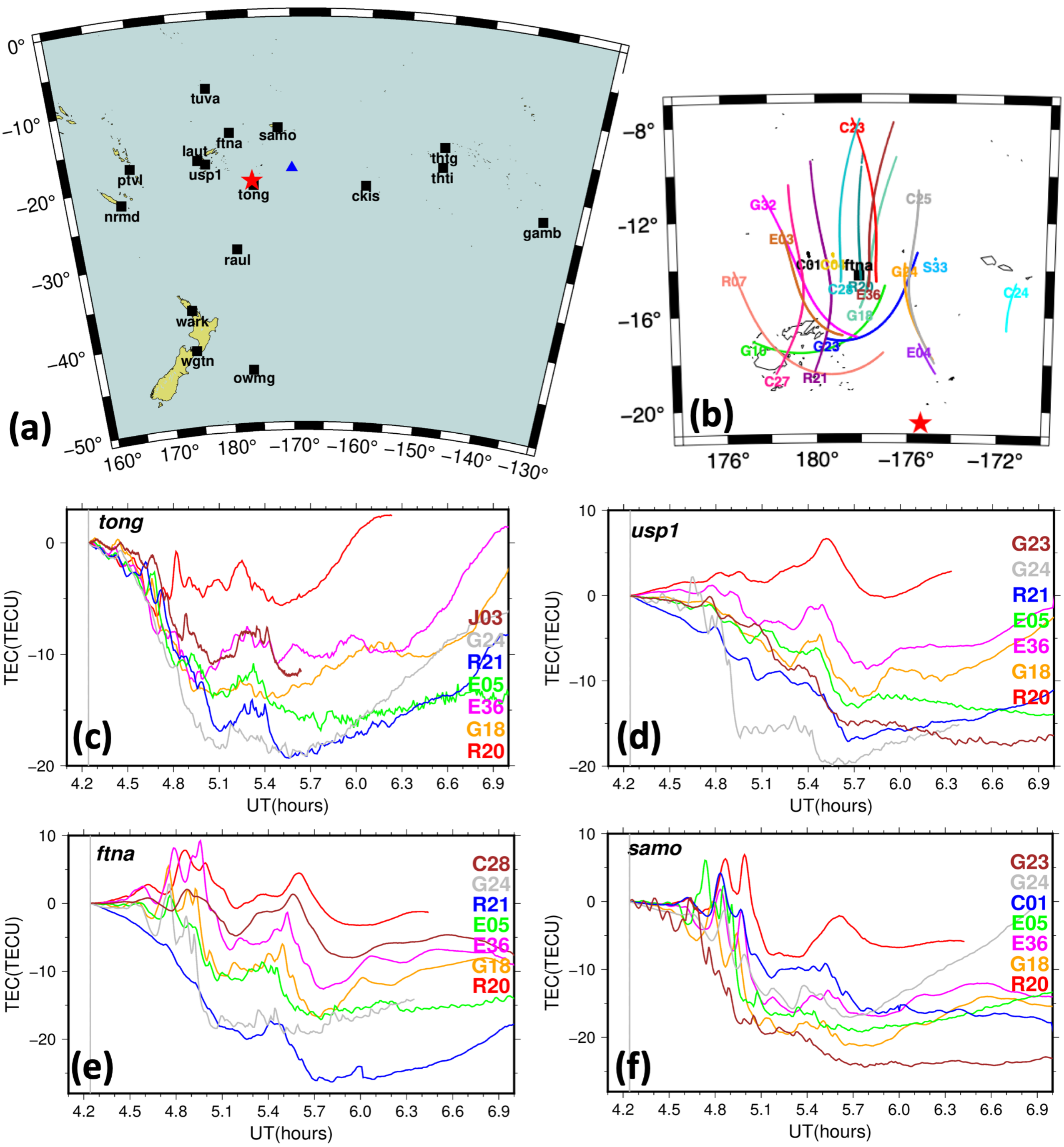

Figure 2. (a) Ionospheric disturbances corresponding to 5 explosions that most likely took place on 15 January 2022. Grey vertical line denotes the USGS onset time; **(b)** Suggested scenario and the timeline of the HTHH volcano explosions of 15 January 2022. Each explosion emits an acoustic pulse of different amplitude as illustrated. Vertical dotted lines correspond to the ionospherically-determined onset times of the explosions.

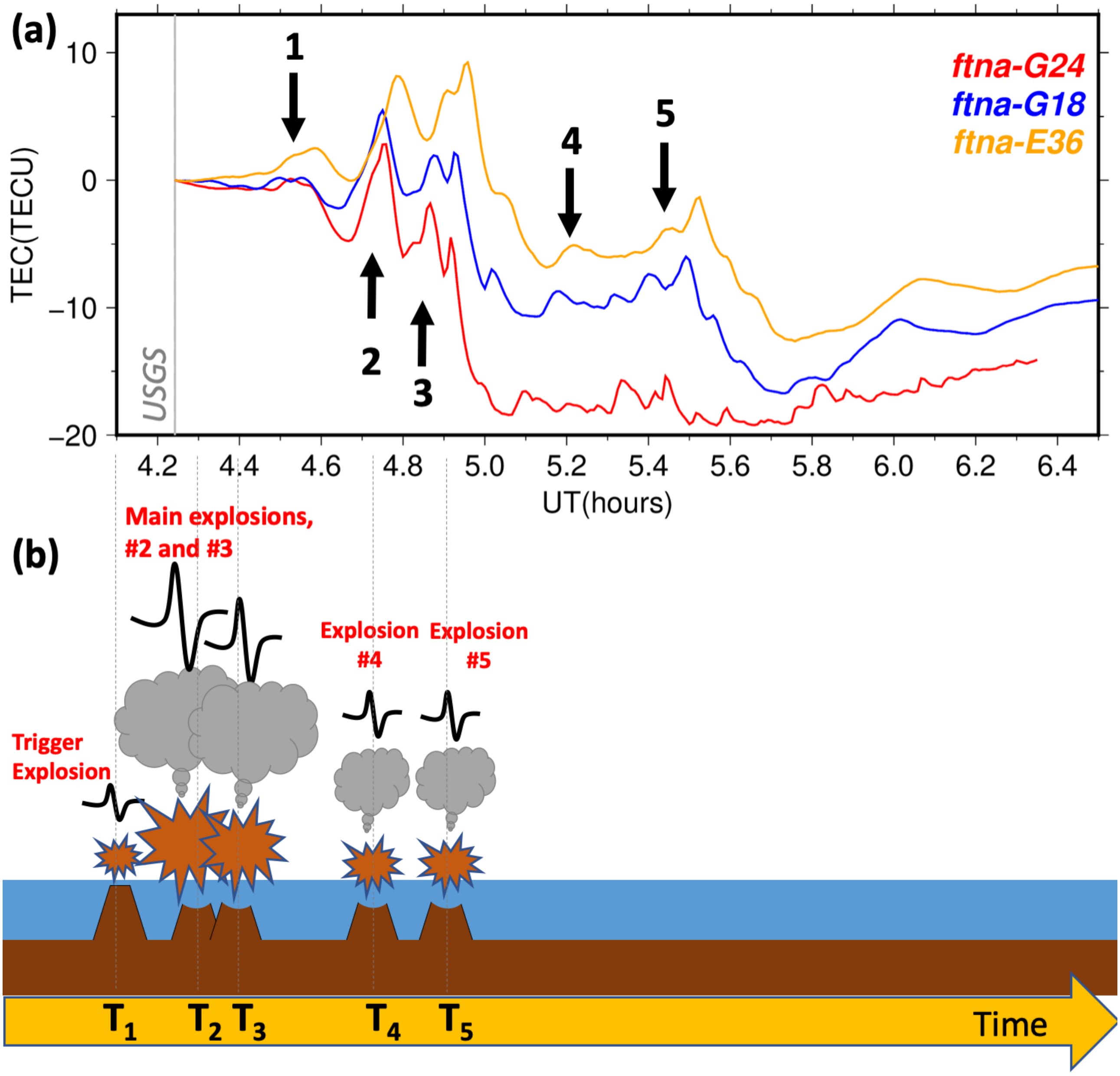

Figure 3. (a) sound speed and **(b)** neutral density profiles used to model the TEC response by using IonoSeis software; **(c)** Comparison of slant TEC observations (gray and black curves) with IonoSeis simulations (red curves) for FTNA-E36, FTNA-G24, FTNA-G18 LOS. The black and grey slant TEC curves have been scaled by the coefficient indicated just above the receiver-satellite pair name. Thin colored curves show different pulses launched at different moments of time as shown on the legend on the right. The dots on the bottom x-axis indicate relative size of source based on a scalar amplitude factor. The numbers are relative to the first event, which has amplitude 1.

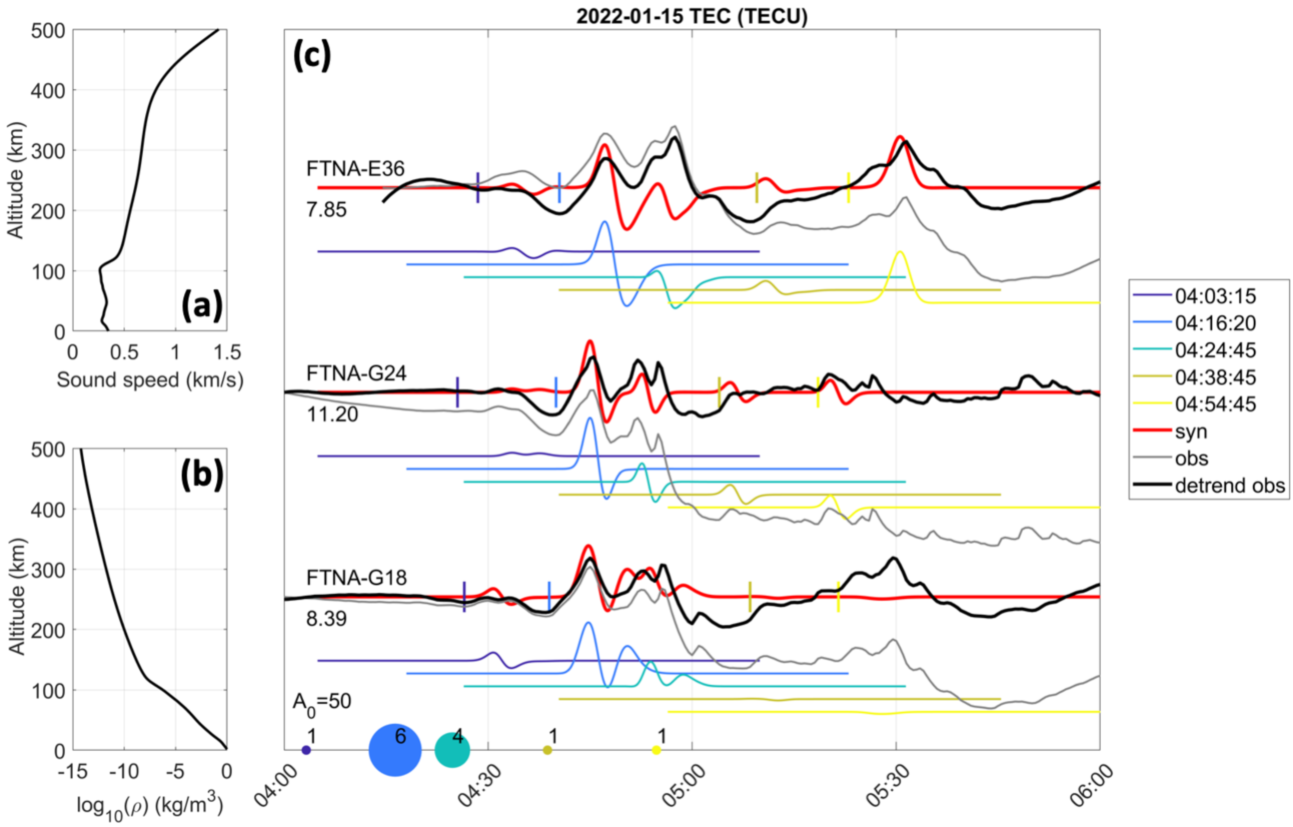

Figure 4. (a-c) Ionospheric depletion as seen on the eruption day (red curve, 015) with respect to four quiet days before (010, 011, 012, 013) and the day after the eruption (016) as recorded by *tong* station and *G24* satellite **(a)**, *tong G23* **(b)**, and *ftna S33* **(c)**. Gray triangles depict the approximate time of the solar terminator; **(d-f)** TEC snapshots plotted by using data of all satellites and all stations shown in Figures 1a-b: **(d)** close to the eruption onset at 04:15UT; **(e-f)** during the depletion observations at 05:00UT and 06:41UT.

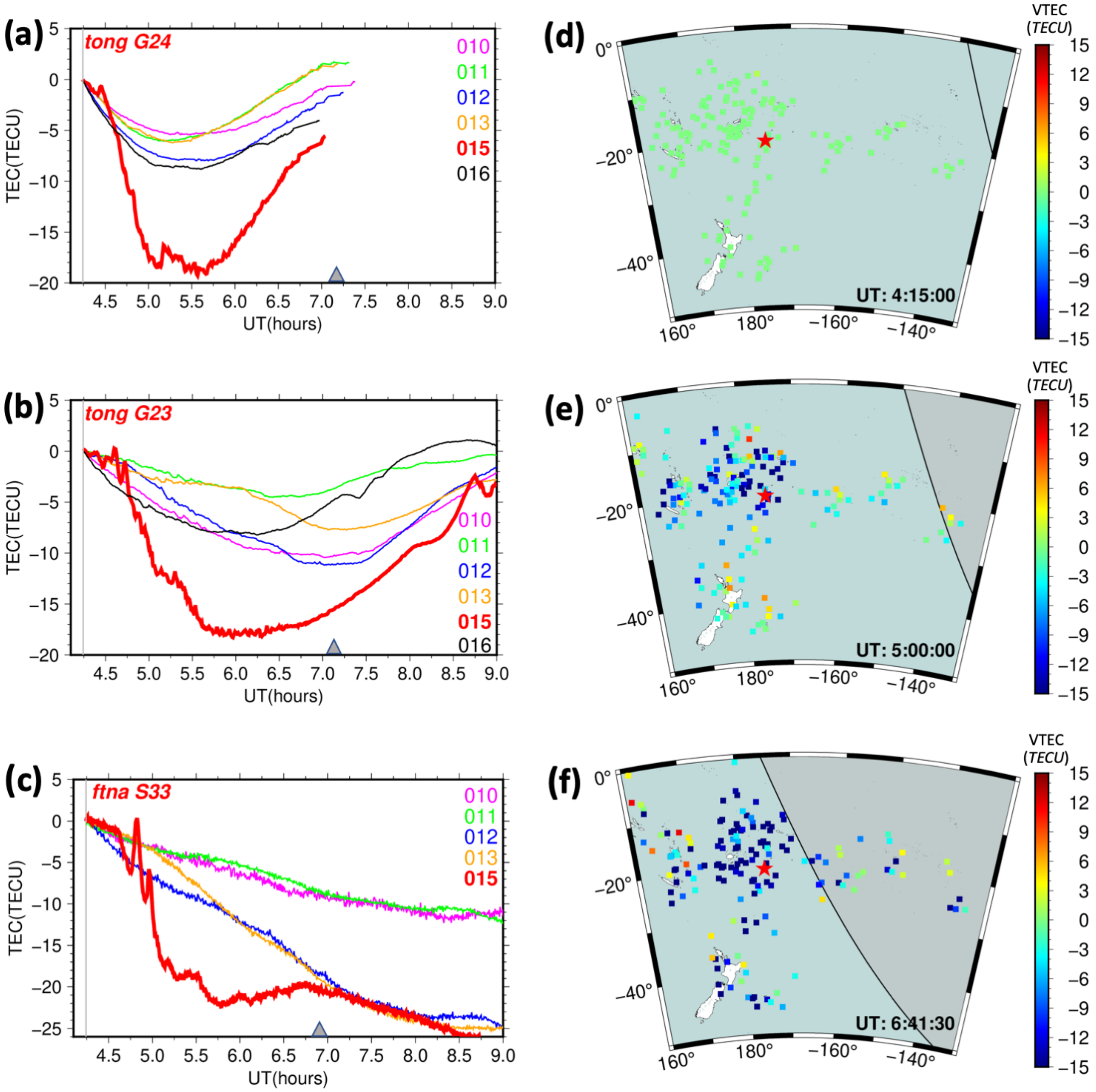

Table 1: Time onsets of the five HTHH volcano explosions as estimated from the ionosphere: by using the approximation of spherical wave at constant radial velocity (columns 4-5), $Onset_{SPHER}$, and by using the IonoSeis software, $Onset_{IonoSeis}$ (column 6). The final ionospheric onset time was calculated by averaging the solutions in columns 5 and 6.

#	Sub-Event	CVID detection time (UT)	CVID radial Velocity (m/s)	$Onset_{SPHER}$ (UT)	$Onset_{IonoSeis}$ (UT)	Onset_iono (UT ± sec)
1	Trigger/initial event	04:20:00, 04:22:30	620	04:08:43	04:03:15	04:05:54±169
2	Main explosion	04:25:30; 04:28:00	620	04:20:00	04:16:20	04:18:10±110
3	Explosion 3	04:51:30; 04:53:00	510	04:28:05	04:24:45	04:26:25±100
4	Explosion 4	05:05:30; 05:07:30	770	04:48:30	04:38:45	04:43:37±292
5	Explosion 5	05:08:30; 05:15:30	550	04:55:21	04:54:45	04:54:27±18

Geophysical Research Letters

Supporting Information for

The 15 January 2022 Hunga Tonga eruption history as inferred from ionospheric observations

E. Astafyeva[1], B. Maletckii[1], T. D. Mikesell[2], E. Munaibari[3], M. Ravanelli[1], P. Coisson[1], F. Manta[3], L. Rolland[3]

1 – Université Paris Cité, Institut de Physique du Globe de Paris (IPGP), CNRS UMR 7154, 35-39 Rue Hélène Brion, 75013 Paris, France, email : astafyeva@ipgp.fr
2 – Norwegian Geotechnical Institute, Natural Hazards, Oslo, Norway
3 – Université Côte d'Azur, Observatoire de la Côte d'Azur, CNRS, IRD, Géoazur, 250 rue Albert Einstein, Sophia Antipolis 06560 Valbonne, France.

Contents of this file

Introduction

The supplementary material consists of Texts S1-S2, Figures S1 – S4 and Tables S1 – S5.

Figure S1 illustrates the method of ionospheric localization of the volcanic source.

Figure S2 shows the travel-time diagrams (hodocrones) for TEC data series measured by four satellites: G24 (a), G23 (b), G18 (c) and R20 (d). One can be clearly see the occurrence of at least 2 main disturbances at ~4.45-4.9 UT and ~5.2–5.7 UT in data of G18 and R20. From the hodocrones, we estimate the apparent velocities to be in the range 555-680 m/s for G23 and G24, 740 m/s for G18 and about 1100 m/s for R20 for both disturbances. We note that this range of velocities correspond to the acoustic waves, which is an additional proof of the observed TEC peaks being driven by explosions.

Figure S3 demonstrates that on the day of the eruption (15 January 2022), the thermospheric composition was decreased over the area of the volcano, as a result of the geomagnetic storm that commenced the day before.

Figure S4 shows TEC variations that capture the response to the explosion at ~08:25UT. This TEC response is very moderate because of the poor ionization due to the large-scale depletion.

Tables S1-S5 present the parameters of CVID used for ionospheric estimation of the onset time for the explosions 1 to 5, respectively, as mentioned in the main text and in Figure 2(b).

All GNSS data are freely available from the CDDIS data archives (https:// https://cddis.nasa.gov/). Data of station RAUL are from the Geological hazard information for New Zealand (GeoNet) FTP-database via ftp://ftp.geonet.org.nz/gps/rinex/. The data of the thermospheric O/N2 composition are available from: http://guvitimed.jhuapl.edu/. The GUVI instrument was designed and built by The Aerospace Corporation and The Johns Hopkins University. The Principal Investigator is Dr. Andrew B. Christensen and the Chief Scientist and co-PI is Dr. Larry J. Paxton.

Text S1

We use an approximation of spherical wave propagating from a point source (*Xs, Ys, Zs*), at constant speed *V* (Kiryushkin & Afraimovich, 2007; Shults et al., 2016). Co-volcanic ionospheric disturbances (CVID) arrive at points (*Xi, Yi, Zi*) at moments of time t_i (Figure S1). The altitude of CVID detection is *Hion* = 320 km, and the source coordinates are taken at the position of the HTHH volcano. First, we find the "reference" point (X_0, Y_0, Z_0) that corresponds to the earliest arrival. Then, we solve a system of equations for the spherical wave travelling from the point source to the reference point (distance $\rho 0$) and to the i_{th} point (distance ρi), and we compute the time delay of the perturbation arrival in registration points. The distance between the reference point and the i_{th} point is determined as *dρi = ρi-ρ0* (Figure S1). These calculations are made for all possible values in the range of velocity *V* between 600 m/s and 1100 m/s, which is in the range of the acoustic wave speed.

For each combination of parameters, we compute an error between the spherical wave model and the real observations, and the result with the minimal value of the error corresponds to the final solution.

The onset time is calculated from the computed parameters: the propagation velocity *V*, the coordinates of the source (*Xs, Ys, Zs*), and the arrival time *t0* of the disturbance in the reference point:

$$\boldsymbol{t_s = t_0 - \frac{\sqrt{(x_0 - x_s)^2 + (y_0 - y_s)^2 + (z_0 - z_s)^2}}{V}} \tag{S1}$$

This method was applied to analyze the scenario of the HTHH eruption of 15 January 2022. We first identified peaks with clear N-wave-like signatures that could correspond to an explosion. We note that not every peak in the TEC data series in Figure 2a corresponds to a separate explosion. Some peaks can be artificially formed by the geometry on the GNSS-sounding (as further seen in the simulation results in Figure 3), or some small peaks can represent the gravity waves generated due to the continuous eruption. For such cases, the approximation of spherical wave will not work.

For each selected sub-event, we estimated the arrival time of the CVID and the coordinates of the CVID detection. Further, we launch our algorithm and we find that the peak between events #3 and #4, and the peak after even #5 do not give any realistic solutions, therefore, we consider that they might not correspond to acoustic waves driven by explosions. Other peaks (noted as 1,2,3,4,5 in Figure 2) provided the onset times and the radial velocity values in the range of acoustic waves (Table 1).

Text S2

We model individual explosive events using the IonoSeis package (Rolland et al., 2013, Mikesell et al., 2019). The ratio of specific heat used to derive the sound speed 1D profile is computed from the composition of the atmosphere provided by NRLMSIS 2.0 model (Emmert et al., 2020) at the time and date of the event. The acoustic shock-wave (bipolar pulse) was taken as the first derivative of a Gaussian pulse (i.e., an N-wave):

$$v(\vec{r},t) = A_z(\vec{r})\frac{A_0\sqrt{2}}{\sigma^{3/2}\pi^{1/4}}(t-t_0)\,e^{-\frac{(t-t_0)^2}{\sigma^2}} \tag{S2}$$

where t_0 is the time of maximum particle motion; σ is the pulse width in seconds; A_0 is the initial amplitude factor, which scales the amount of energy injected in the atmosphere from the point source (Dautermann et al., 2009; Mikesell et al., 2019); and *Az* is an amplitude factor that describes how the phase and amplitude are affected by frequency-dependent viscous and thermal losses with altitude. The broadening of the pulse due to dispersion upon its propagation is taken into account as:

$$\sigma(\vec{r},t) = bt_w \tag{S3}$$

where *b* is a scale factor so that the pulse width increases with propagation time. Here *b* was set to 0.04 except the third event that has a *b* factor of 0.01.

The initial atmosphere model is in steady state for each individual simulation. Therefore, we know that at later times after the ionosphere has been disturbed, for instance after the large shock wave, that our initial model is likely incorrect. Therefore, in this study we do not put emphasis on matching the shape of N-waves at later times. This will be the study of future work on the IonoSeis package. However, at early time when our initial model is more valid we do expect to be able to match not just arrival times, but also the waveform shape by adjusting the amplitude (A_0) and the broadening factor *b* (see Mikesell et al. (2019) for more information on modeling parameters).

Figures

Figure S1: (a) Approximation of a spherical wave propagating at a constant speed from a point source with coordinates (*Xs, Ys, Zs*). The eruption onset time is *Ts*. The CVID are detected at points (*Xi, Yi, Zi*) at time moments t_i. The altitude of CVID detection is *Hion* = 320 km; **(b)** Detection points are defined at the moment of time when the TEC starts to significantly increase. For these points, we find the coordinates at the altitude of 320 km. These parameters are further used for the spherical wave algorithm to determine the onsets of the sub-events. Smaller peaks between events 3 and 4, and the peak after event 5 did not give solutions within the spherical wave approximation.

(a)

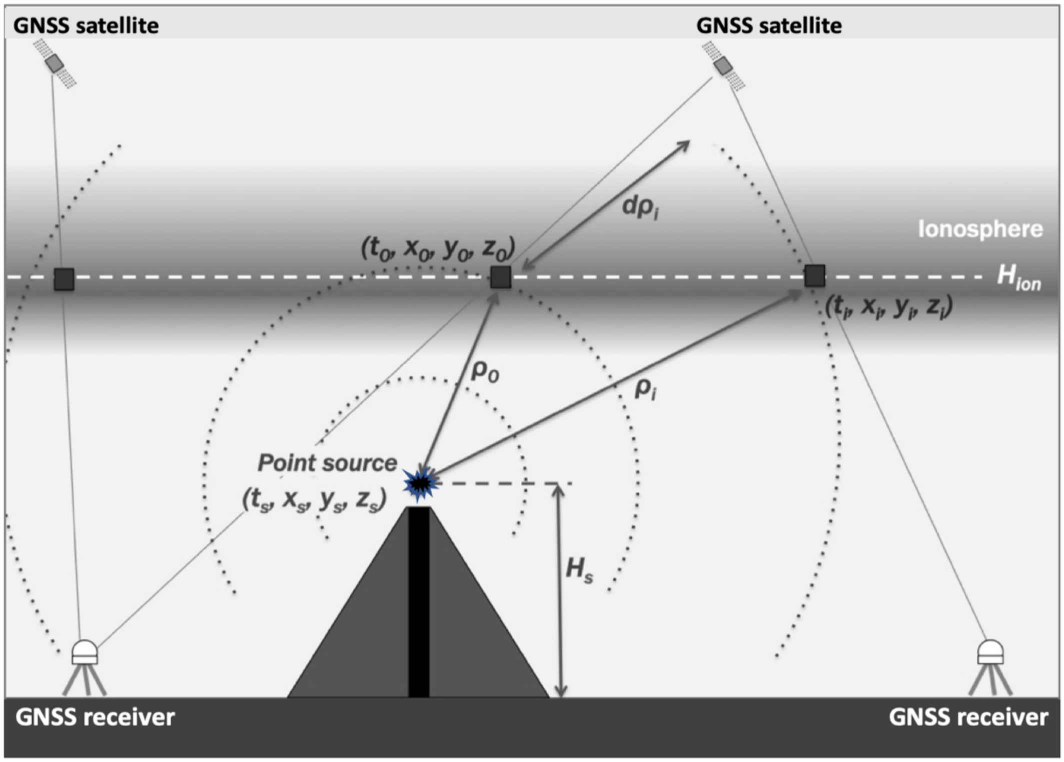
GNSS satellite
GNSS satellite
$d\rho_i$
Ionosphere
(t_0, x_0, y_0, z_0)
H_{ion}
(t_i, x_i, y_i, z_i)
ρ_0
ρ_i
Point source
(t_s, x_s, y_s, z_s)
H_s
GNSS receiver
GNSS receiver

(b)

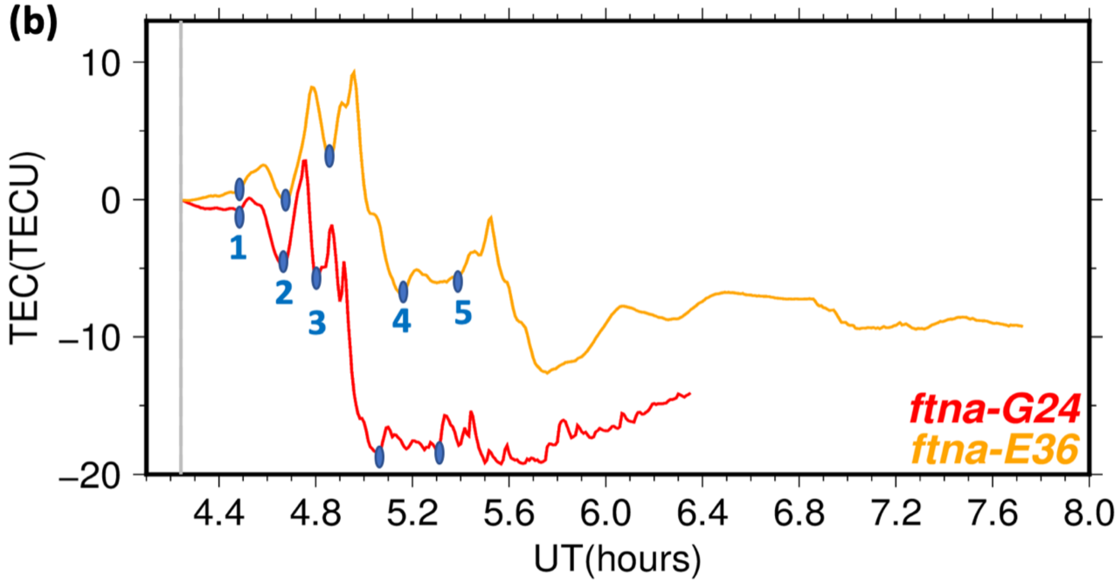
TEC(TECU)
UT(hours)
ftna-G24
ftna-E36
1
2
3
4
5

Figure S2: Travel-time diagrams (hodocrones) for relative unfiltered VTEC for satellites G24 **(a)**, G23 **(b)**, G18 **(c)** and R20 **(d)**. The apparent velocities are 680 m/s (a), 555 m/s (b), 740 m/s (c) and 1100 m/s (d).

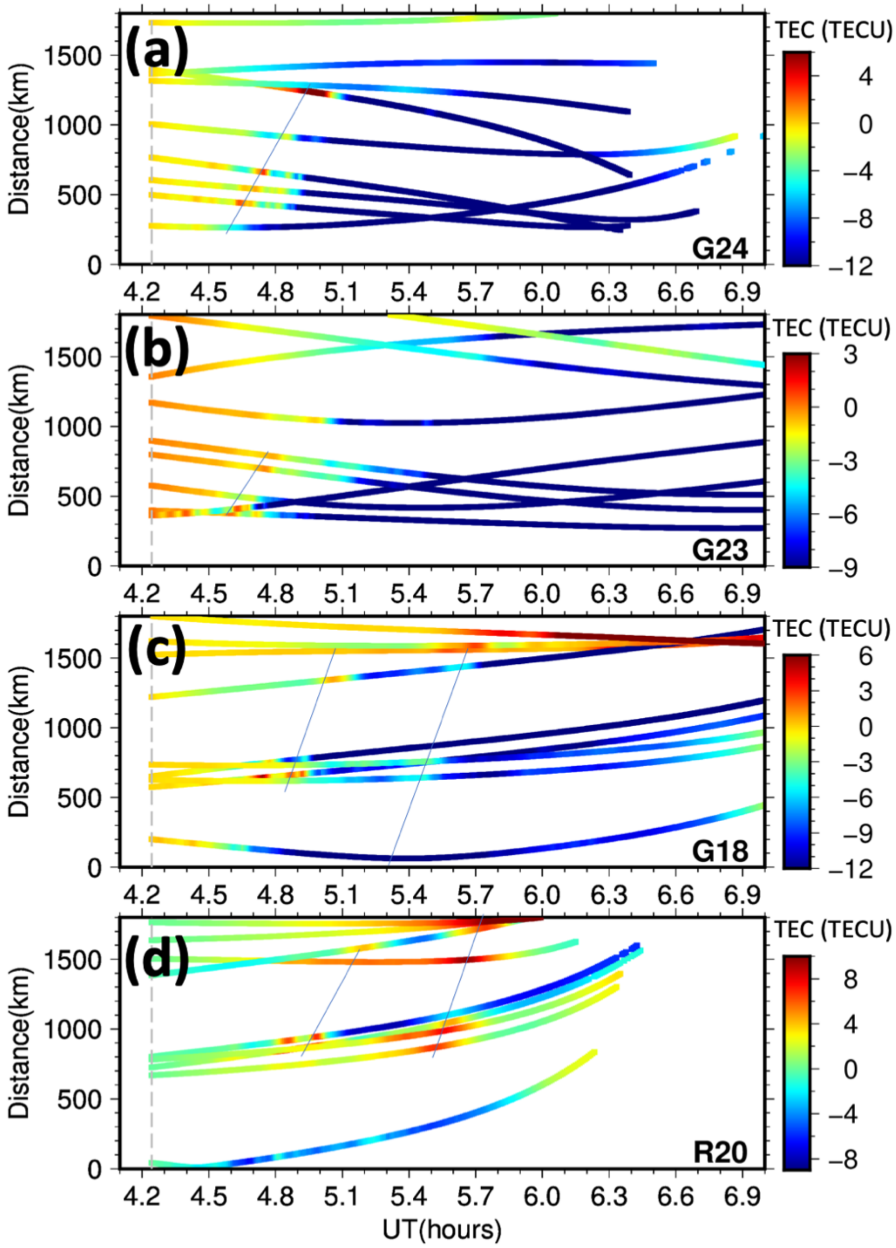

Figure S3: Thermospheric O/N2 composition changes on 13-16 January 2015. The GUVI instrument measures a narrow swath below the satellite at 625 km altitude during the dayside spacecraft passages [Christensen et al, 2003]. The figures show O/N2 data smoothed over 14.9 daily orbits. Red circle in lower left indicates the volcano position (175.382W; 20.536S). We suspect that the composition changes reinforced the ionospheric TEC depletion that was produced by the eruption-driven shock wave. It is known that the composition has a drastic impact on the ionization (Prölss, 1976; Fuller-Rowell et al., 1994). An increase in the molecular species causes an increase in the ionization loss rate, and a decrease of atomic oxygen causes a decrease of the ionization production rate; both these phenomena lead to the ionization decrease.

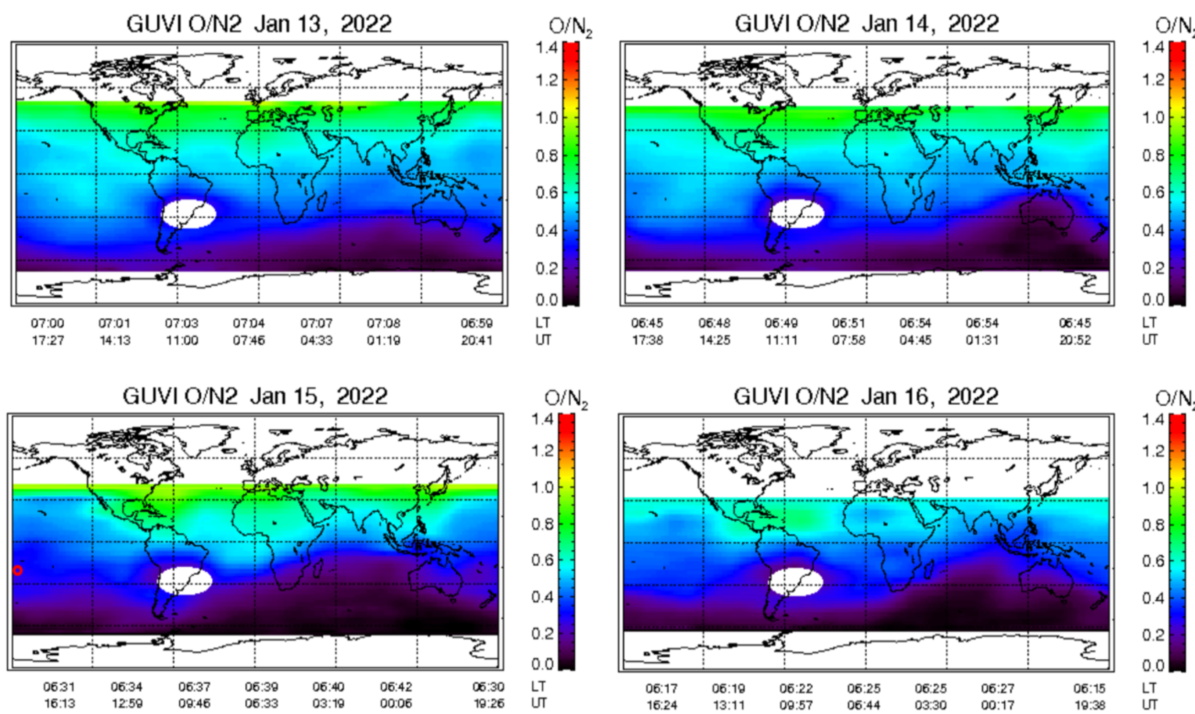

Figure S4: Ionospheric TEC series showing the response to the event that apparently took place ~8:25UT. Arrows show the CVID. We could not analyze this event in detail at this time.

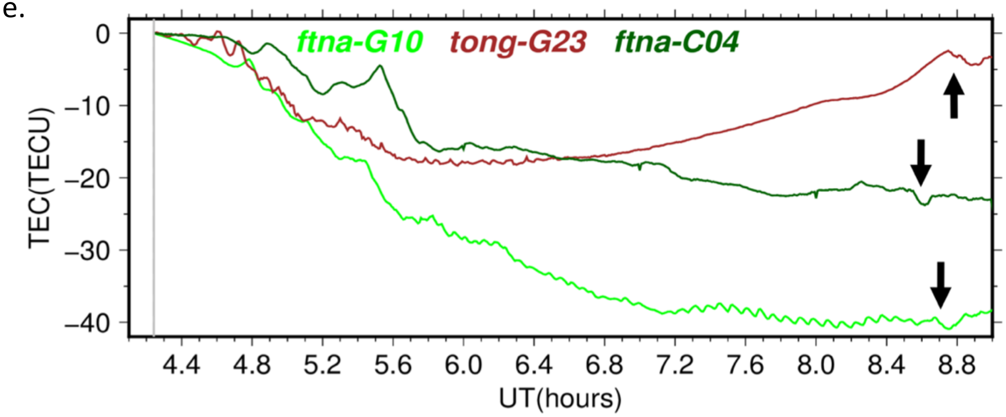

Tables

Table S1: Parameters of the first explosion (marked as #1 in Figure 2b) and the first CVID arrivals (LOS, arrival time Tarr in 30-sec epochs and the coordinates) that were used for estimation of the time onset of this explosion.

LOS	**Tarr (30-sec epoch)**	**CVID arrival (Lon; Lat)**
tong G18	527	184.807899; -22.129765
ftna G18	533	182.068450; -15.712337
samo G18	536	188.093275; -15.246549
tong G24	520	187.182446; -20.184082
usp1 G24	523	181.408881; -17.465429
laut G24	525	180.509488; -17.001210
ftna G24	531	184.382928; -14.003524
samo G24	554	190.173092; -13.874976
tuva G24	569	181.980145; -9.247600
tong E36	525	185.187366; -21.147390
usp1 E36	535	179.212216; -18.247160
ftna E36	537	182.422515; -14.607802
samo E36	540	188.419278; -14.132946

Table S2: Parameters of the arrivals of the explosion #2 (LOS, arrival time Tarr in 30-sec epochs and the coordinates) that were used for estimation of the time onset of this explosion.

LOS	Tarr (30-sec epoch)	CVID arrival (Lon; Lat)
tong E36	536	185.196055 -21.030285
usp1 E36	560	179.233677 -17.973405
ftna E36	561	182.433704 -14.346967
samo E36	570	188.422216 -13.809916
tong G18	554	184.934439 -21.797559
ftna G18	558	182.183594 -15.379847
samo G18	561	188.198567 -14.906396
tong G24	531	187.165347 -20.359883
usp1 G24	554	181.365958 -17.979022
laut G24	555	180.469822 -17.503483
ftna G24	560	184.384855 -14.451798
samo G24	574	190.191415 -14.159892
tuva G24	588	182.027249 -9.569821

Table S3: Parameters of the arrival of the disturbance #3 (LOS, arrival time Tarr and the coordinates) that were used for estimation of the time onset of this explosion.

LOS	Tarr (30-sec epoch)	CVID arrival (Lon; Lat)
ftna E36	583	182.438294 -14.105951
samo R20	593	187.850709 -12.739478
samo G24	593	190.219516 -14.433240
usp1 R20	586	178.735076 -16.851442
usp1 E36	583	179.247208 -17.715818

Table S4: Parameters of the arrival of the sub-event #4 (LOS, arrival time Tarr and the coordinates) that were used for estimation of the time onset of this explosion.

LOS	Tarr (30-sec epoch)	CVID arrival (Lon; Lat)
ftna G24	608	184.447810 -15.201575
ftna G18	617	182.371307 -14.619722
ftna E36	619	182.438051 -13.701351
samo G24	616	190.270918 -14.772845
samo E36	616	188.409984 -13.315402
samo G18	611	188.342906 -14.256654

Table S5: Parameters of the arrival of the sub-event #5 (LOS, arrival time Tarr in 30-sec epoch time and the coordinates) that were used for estimation of the time onset of this explosion in the approximation of a spherical wave propagation.

LOS	**Tarr (30-sec epoch)**	**CVID arrival (Lon; Lat)**
tong G24	617	187.149439 -21.640964
raul G24	660	184.813518 -29.884852
laut G24	631	180.528565 -18.763369
ftna G24	637	184.537825 -15.684248
samo R20	645	187.762099 -11.706563
ftna G18	643	182.429305 -14.286506
ftna E36	646	182.434860 -13.383897
usp1 E36	637	179.266049 -17.073611
usp1 G18	634	179.215389 -18.010305
ftna R20	636	181.866997 -12.334771

References

Christensen, A. B., et al. (2003), Initial observations with the Global Ultraviolet Imager (GUVI) on the NASA TIMED satellite mission, *J. Geophys. Res.*, 108(A12), 1451, doi:10.1029/2003JA009918.

Dautermann, T., E. Calais, and G. S. Mattioli (2009), Global Positioning System detection and energy estimation of the ionospheric wave caused by the 13 July 2003 explosion of the Soufrière Hills Volcano, Montserrat, *J. Geophys. Res.*, 114, B02202, doi:10.1029/2008JB005722.

Emmert, J. T., Drob, D. P., Picone, J. M., Siskind, D. E., Jones, M. Jr., Mlynczak, M. G., et al. (2020). NRLMSIS 2.0: A whole-atmosphere empirical model of temperature and neutral species densities. *Earth and Space Science*, 7, e2020EA001321. https://doi.org/10.1029/2020EA001321

Fuller-Rowell, T. J., Codrescu, M. V., Moffett, R. J., & Quegan, S. (1994). Response of the thermosphere and ionosphere to geomagnetic storms. *Journal of Geophysical Research*, 99(A3), 3893–3914. https://doi.org/10.1029/93JA02015

Kiryushkin, V.V. and E.L. Afraimovich (2007) Determining the Parameters of Ionospheric Perturbation Caused by Earthquakes Using the Quasi-Optimum Algorithm of Spatiotemporal Processing of TEC Measurements, *Earth Planets Space*, 2007, vol. 59, pp. 267–278.

Mikesell, T.D.; Rolland, L.M.; Lee, R.F.; Zedek, F.; Coïsson, P.; Dessa, J.-X. (2019) *IonoSeis*: A Package to Model Coseismic Ionospheric Disturbances. *Atmosphere*, *10*, 443. https://doi.org/10.3390/atmos10080443

Pröss, G. W. (1976) On explaining the negative phase of ionospheric storms, Planet. Space Sci., 24, 607-609.

Rolland, L. M., M. Vergnolle, J.-M. Nocquet, A. Sladen, J.-X. Dessa, F. Tavakoli, H.R. Nankali, and F. Cappa (2013), Discriminating the tectonic and non-tectonic contributions in the ionospheric signature of the 2011, Mw7.1, dip-slip Van earthquake, Eastern Turkey, *Geophys. Res. Lett.*, 40, doi:10.1002/grl.50544.

Shults, K., E. Astafyeva and S. Adourian (2016). Ionospheric detection and localization of volcano eruptions on the example of the April 2015 Calbuco events. *J. Geophys. Res. - Space Physics*, V.121, N10, 10,303-10,315, doi:10.1002/2016JA023382.